Biomineralization of Bi_2S_3-Gd_2O_3 nanocomposites: a novel approach for enhanced photothermal and MRI applications

Q. Lu [a], B. H. Zhang [b], T. H. Yi [a], L. G. Hao [a], J. L. Xue [a], W. B. Duan [a], Y. G. Wan [a], D. T. Chen [a], J. Wang [a], X. Guo [a], L. P. Zhang [a,*]

[a] *Department of Molecular Imaging, School of Medical Technology, Qiqihar Medical University, Qiqihar 161042, China*

[b] *Department of Clinical Medicine, School of General Medicine, Xinjiang Medical University, Urumqi 830054, China*

In this study, Bi_2S_3-Gd_2O_3 nanocomposites (Bi_2S_3-Gd_2O_3@BSA) were prepared via biomineralization using albumin as a template, and the nanomaterials were directed to the tumor site through surface folic acid modification. Among these materials, Bi_2S_3 serves as an effective photothermal conversion agent (PTA) for photothermal therapy at tumor sites, attributed to its impressive photothermal conversion efficiency. In contrast, Gd_2O_3, being a paramagnetic substance, can serve effectively as a contrast agent in the magnetic resonance imaging (MRI). According to in vitro and in vivo experiments, the nanomaterials exhibit low toxicity, favorable biocompatibility, and outstanding photothermal properties. Upon the exposure to 808 nm laser irradiation, the nanomaterials quickly reach the therapeutic temperature necessary for effective tumor treatment. With folic acid modification, these nanomaterials accumulate in the tumor region, enabling efficient treatment. This strategy provides a fresh outlook for the purposeful design of diagnostic agents aimed at tumor imaging and therapy.

(Received October 9, 2024; Accepted December 9, 2024)

Keywords: Bismuth sulfide, Folic acid, Photothermal therapy, Nano, MR imaging

1. Introduction

Colorectal cancer (CRC) is a representative malignant tumor, accounting for 9.4% of cancer deaths in 2020, with its prevalence estimated to increase by 3.2 million by 2040 [1]. In addition to traditional CRC treatments such as radiotherapy, chemotherapy, and surgery, novel therapeutic options—including hemodynamic therapy [2-4], immunotherapy [5], and photothermal therapy [6-8]—offer additional clinical possibilities. As molecular imaging technology advances, conventional magnetic resonance imaging (MRI) contrast agents no longer meet clinical requirements, making it necessary to develop a nano-platform integrating both diagnosis and treatment [9-11]. Photothermal

* Corresponding author: zhangliping@qmu.edu.cn
https://doi.org/10.15251/DJNB.2024.194.1903

therapy (PTT) adopts external light to achieve the light energy-to-thermal energy conversion, with a photothermal agent (PTA) localizing at the tumor site, killing tumor cells via localized heating, offering a non-invasive treatment method [12, 13]. In photothermal therapy, the PTA is pivotal, and PTAs are generally classified into two major categories: organic and inorganic [14]. Organic agents often suffer from poor photothermal stability and low intratumoral accumulation, whereas inorganic agents, typically comprising metals of gold (Au)[15, 16], silver (Ag)[17, 18], palladium (Pd)[19, 20], and tungsten (W)[21, 22], achieve photothermal conversion via surface plasmon resonance (SPR), offering superior photothermal stability and conversion efficiency[23, 24]. Bismuth-based metallic nanomaterials, including bismuth nanoparticles (Bi)[25, 26], bismuth sulfide (Bi_2S_3)[27, 28], and bismuth selenide (Bi_2Se_3)[29, 30], are promising alternatives for photothermal conversion due to their high near-infrared absorption coefficients.

Therefore, a nanomaterial was synthesized using BSA as a sulfur source. In this nanosystem, Bi_2S_3 synthesized through biomineralization functions as a photosensitizer, Gd^{3+}enables MRI, and folic acid serves as a targeting molecule to direct the system to the tumor site. Following intravenous injection of FA-Bi_2S_3-Gd_2O_3@BSA nanomaterials, effective aggregation occurred in mice due to FA-assisted targeting (Scheme 1). According to subsequent in vitro and in vivo studies, FA-Bi_2S_3-Gd_2O_3@BSA nanomaterials exhibited strong PTT effects under MRI guidance, effectively suppressing tumor growth in a mouse model of CRC.

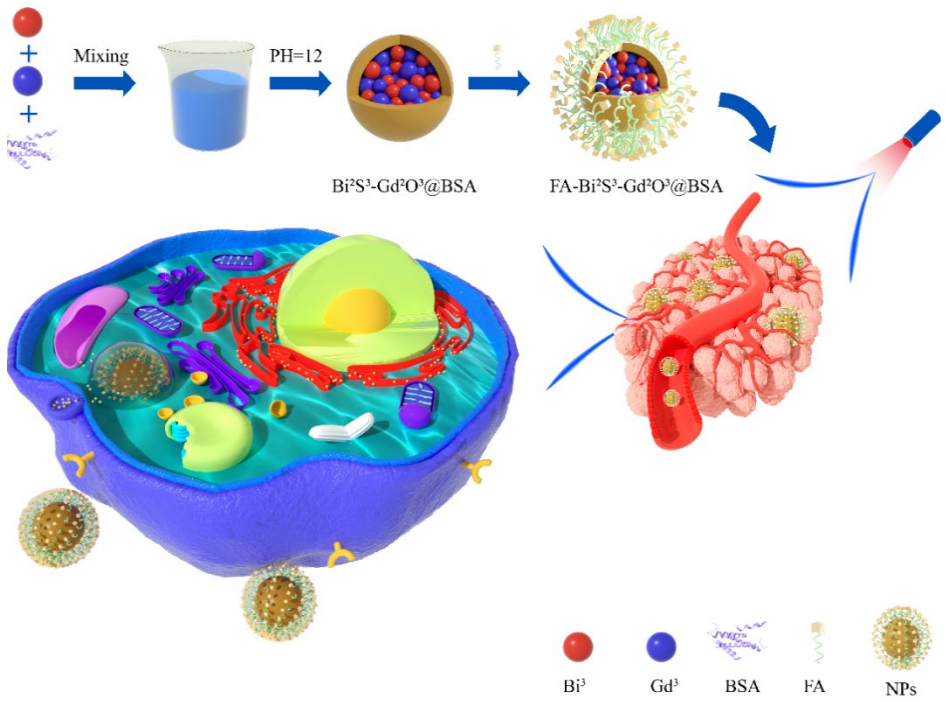

Scheme 1. Synthesis process of FA-Bi_2S_3-Gd_2O_3@BSA.

2. Materials and methods

2.1. Materials

Bismuth nitrate, gadolinium chloride, BSA, sodium hydroxide, and DMSO were provided by Aladdin; FA, EDC, and NHS were obtained from Picasso; FITC was sourced from McLean; a dialysis bag was acquired from Beijing Kulaibo; McCoy's 5A, serum, double antibody, trypsin, and PBS were purchased from Hycyte; DAPI was sourced from Boeotopia, and the live-dead cell kit was acquired from Biyuntian.

2.2. Synthesis of Bi_2S_3-Gd_2O_3@BSA

To prepare the solution, experimenters mixed 500 mg of BSA with 10 mL of deionized water, meanwhile dissolving 0.025 mmol of $Bi(NO_3)_3 \cdot 5H_2O$ in 1 mL of a 2 M HNO_3 solution. Once both components were completely dissolved, the $Bi(NO_3)_3$ solution was gradually added to the BSA solution. Following this, 1 mL of 25 mM $GdCl_3 \cdot 6H_2O$ was added dropwise while continuously shaking and mixing the solution. After the dropwise addition was finished, the solution was added with 2 M NaOH to modify the pH to 12, followed by being agitated at room temperature for a duration of 12 hours and subjected to hydrolysis for 48 hours to purify it. Finally, the solution was thoroughly mixed again with the BSA aqueous solution.

2.3. Synthesis of FA-Bi_2S_3-Gd_2O_3@BSA

10 mg each of FA, EDC, and 6 mg of NHS were carefully weighed and dissolved in 5 mL of DMSO. This solution underwent 1 h of stirring at room temperature while being protected from light. Following this initial preparation, the Bi_2S_3-Gd_2O_3@BSA solution (10 mg/mL) was added slowly, and the mixture underwent another 12 h of stirring, again shielded from light. Subsequently, dialysis was carried out with a dialysis bag (molecular weight cutoff: 12 kDa), resulting in the purification of FA-Bi_2S_3-Gd_2O_3@BSA.

2.4. Characterization

A high-resolution transmission electron microscopy (HRTEM, JEM-2100Plus) was applied for the nanomaterial examination in terms of the structures and dimensions, an X-ray photoelectron spectroscopy (XPS, Thermo ESCALAB 250XI) was employed for the evaluation of the chemical states and composition, and an X-ray diffractometer (Smartlab SE, Rigaku) was employed to evaluate the crystalline characteristics. A (Nicomp-380ZLS) particle size analyzer served for measuring the hydrated particle size and zeta potential. The collection of Fourier Transform Infrared (FT-IR) spectra relied on an FT-IR Spectrometer (EQUINOX 55, Bruker). The last procedure was the confirmation of the bismuth and gadolinium concentrations in the materials using the inductively coupled plasma mass spectrometry (ICP-MS, Agilent 7800).

2.5. Photothermal performance

With the aim of assessing the materials' photothermal properties, we prepared an aqueous dispersion of Bi_2S_3-Gd_2O_3@BSA at varying Bi^{3+} concentrations, with 1 mL of the solution placed into a quartz cuvette. This setup was irradiated vertically for 10 minutes using an 808 nm laser (power density: 1 W/cm²). Temperature readings were captured at 30-second intervals with an infrared thermography camera. Furthermore, to assess photothermal stability, we extracted 1 mL of

the Bi_2S_3-Gd_2O_3@BSA dispersion solution (Bi^{3+} concentration: 120 μg/mL) into a quartz dish, and subsequently, irradiated it vertically with a laser of power 1 W/cm^2 for 10 minutes. After 10 min of natural cooling, solution underwent another time of laser irradiation, and the operation repeated five times, with the temperature change measured each time.

Equation blow explains the photothermal conversion efficiency:

$$\eta = \frac{\mathrm{h}S(T_{max} - T_{surr}) - Q_0}{\mathrm{I}(1 - 10^{-A_\lambda})}$$

2.6. Cytotoxicity

The HT-29 cell line was acquired from Hycyte. HT-29 cells (1×10^4 cells/well) underwent 24 and 48 h of co-culture with FA-Bi_2S_3-Gd_2O_3@BSA solution (Bi^{3+} concentrations: 10, 50, 100, 150, 200, 250, 300 μg/mL). The CCK-8 assay assisted in the cell viability evaluation. Each group was subjected to 3 independent experiments for guaranteeing the result reliability.

2.7 Cell uptake assay

Confocal laser scanning microscopy (CLSM) was used for qualitative studies, while flow cytometry was employed for quantitative studies, aiming at evaluating the cellular uptake of Bi_2S_3-Gd_2O_3@BSA and FA-Bi_2S_3-Gd_2O_3@BSA. HT-29 cells, grown to logarithmic phase, were seeded (1×10^5 cells/well) in culture dishes suitable for CLSM analysis. After the cells adhere, add Bi_2S_3-Gd_2O_3@BSA-FITC and FA-Bi_2S_3-Gd_2O_3@BSA-FITC to each well, incubate for 4 hours, and then fix with paraformaldehyde (PFA, 4%) for 10 minutes. Subsequently, the DAPI reagent was added under light-avoidance conditions and incubated for 10 minutes before fluorescence images were obtained using CLSM. Additionally, quantitative intracellular uptake of FA-Bi_2S_3-Gd_2O_3@BSA and Bi_2S_3-Gd_2O_3@BSA was analyzed using flow cytometry. This was accomplished by incubating the cells with Bi_2S_3-Gd_2O_3@BSA-FITC or FA-Bi_2S_3-Gd_2O_3@BSA-FITC, digesting them with 0.25% trypsin, suspending them in PBS, and detecting the cellular uptake rate using flow cytometry.

2.8 Hemolysis experiment

To assess the blood compatibility of Bi_2S_3-Gd_2O_3@BSA nanomaterials, the hemolysis rate of erythrocytes was measured. The specific experimental methods included the following: 2 mL of whole blood was drawn from mice and transferred into anticoagulant tubes containing heparin. The samples underwent 10 min of rotation at 2000 rpm, and the erythrocytes were isolated after the elimination of the supernatant. The isolated erythrocytes were then dispersed in 20 mL of PBS for further use. That was followed by the addition of a volume of 200 μL of red blood cell (RBC) suspension to a centrifuge tube to be mixed with Bi_2S_3-Gd_2O_3@BSA dispersions at varying concentrations (25-500 μg/mL). Deionized water and PBS respectively served as a positive control and a negative control. The mixed samples were then placed in a 37°C water bath to receive 2 h of incubation. After the incubation, each sample underwent 10 min of centrifugation at 12,000 rpm, followed by the transfer of 200 μL of the supernatant from each sample to a 96-well plate. A microplate reader was used for the measurement of the absorbance at 570 nm. The formula below calculates the hemolysis rate:

$$\text{hemolysis rate}(\%) = \frac{\mathrm{A_{NPs}} - \mathrm{A_{PBS}}}{\mathrm{A_{water}} - \mathrm{A_{PBS}}} \times 100\%$$

where, A_{NPs} denotes the absorbance of various concentrations of nanomaterials, A_{PBS} refers to the absorbance of the PBS group, while A_{water} indicates the absorbance of the deionized water group.

2.9. Animal experiments

Female BALB/c nude mice (aged 4 to 6 weeks) came from Liaoning Changsheng Biotechnology. All animal experiments followed the approved guidelines of the Animal Ethics and Use Committee at Qiqihar Medical University. Throughout the study, the mice were housed in a controlled sterile condition (temperature: 22 ± 1 ℃; relative humidity: 50% to 60%). Each mouse was administered 1×10^6 HT-29 cells suspended in 100 μL of NaCl by subcutaneous injection into right forelimb, so as to build the tumor model. In the case the tumor volume reaching approximately 200 mm^3, the mice will be treated.

2.10. In vivo imaging of FA- Bi_2S_3-Gd_2O_3@BSA

FA-Bi_2S_3-Gd_2O_3 solutions with different concentrations (Gd^{3+} concentration: 0.12-1.92 mM) were prepared and placed into the NMR analyzer to measure the longitudinal relaxation time. The FA-Bi_2S_3-Gd_2O_3 concentration was plotted as the horizontal coordinate (X), while the reciprocal of the longitudinal relaxation time ($1/T_1$) was plotted as the vertical coordinate. The concentration of Gd_2O_3@BSA was plotted against the longitudinal relaxation intensity to generate corresponding curves. To verify the MRI capability of the nanomaterials, the aforementioned concentration gradients were arranged in ascending order, and T_1 imaging relied on a Philips 3.0 T MRI scanner.

For in vivo MRI, the mice were administered 200 μL of FA-Bi_2S_3-Gd_2O_3@BSA and Bi_2S_3-Gd_2O_3@BSA dispersions (Bi^{3+} concentration: mg/mL) by tail vein injection, followed by being placed in a gas anesthesia device for complete anesthesia and subsequently positioned in a Philips 3.0T MRI scanner for MR examinations before drug administration, and at 1, 3, 5, and 8 hours after administration. The scanning sequence and related parameters were as follows: T_1-weighted imaging (axial and coronal): TR = 450-650 ms, TE = 10 ms.

2.11. Histological analysis

Following the treatment, healthy Balb/c mice that had not undergone any treatment were designated as the control group. We collected tumor tissues, along with organs of heart, liver, spleen, lungs, and kidneys from the nude mice in each group. These tissue specimens, after fixed in 4% PFA, underwent paraffin-embedding, and section pathological examination. Subsequently, the sections received H&E staining. Finally, the therapeutic efficacy of the nanomaterials was assessed through histopathological analysis.

2.12. Photothermal treatment of tumor cells in vitro

To examine the cytotoxic effects of Bi_2S_3-Gd_2O_3@BSA nanomaterials on cancer cells under light conditions, a live-dead double staining method was employed for cell labeling. A Bi_2S_3-Gd_2O_3@BSA dispersion, containing 120 μg/mL of Bi^{3+}, was incubated with the HT-29 cells for 24 hours. After the incubation, the cells received 10 min of laser irradiation at 808 nm (1 W/cm^2). The cells were subsequently stained and fixed using the two-dye agents Calcein AM and Propidium Iodide (PI), and then observed under an inverted fluorescence microscope. The experimental groups were organized as follows: (i) control group, (ii) laser group, (iii) Bi_2S_3-Gd_2O_3@BSA group, (iv) FA-Bi_2S_3-Gd_2O_3@BSA group, (v) Bi_2S_3-Gd_2O_3@BSA + laser group, and (vi) FA-Bi_2S_3-Gd_2O_3@BSA + laser group. Each group received the same culture and staining treatment. To more intuitively illustrate the photothermal killing effect of Bi_2S_3-Gd_2O_3@BSA nanomaterials on cancer cells, dispersions of Bi_2S_3-Gd_2O_3@BSA (120 μg/mL) and FA-Bi_2S_3-Gd_2O_3@BSA (120 μg/mL)

were subjected to 24 h of culture using HT-29 cells in 96-well plates. Subsequently, the cells underwent 0, 3, 7, and 10 min of irradiation with an 808 nm laser (1 W/cm²). Finally, the CCK-8 kit served for cell viability assessment in each group.

2.13. Photothermal treatment of tumors in vivo

In the case of the tumor volume reaching 200 mm³, the nude mice are assigned to six groups in a random manner (n = 3): (i) control group, (ii) laser group, (iii) Bi_2S_3-Gd_2O_3@BSA group, (iv) FA-Bi_2S_3-Gd_2O_3@BSA group, (v) Bi_2S_3-Gd_2O_3@BSA + laser group, and (vi) FA-Bi_2S_3-Gd_2O_3@BSA + laser group. The (i) and (ii) groups received saline injections, while the (iii) and (v) groups received Bi_2S_3-Gd_2O_3@BSA injections, and the (iv) and (vi) groups received FA-Bi_2S_3-Gd_2O_3@BSA injections. Two hours after the injections, the (ii), (v), and (vi) groups underwent 10 min of irradiation with an 808 nm laser (1 W/cm²), during which a thermal imaging camera recorded and monitored the temperature fluctuations at the tumor sites of the mice in real time. Measurement was conducted on the mice's body weight each two days after the conclusion of treatment. Vernier calipers were used to precisely measure the longest diameter (a) and the shortest diameter (b) of the tumors. Calculation formula of the tumor volume is as follows:

$$V = \frac{ab^2}{2}$$

2.14. Statistical analysis

Statistical analysis on experimental data relied on GraphPad Prism 9.5 and Origin 2024 software. Data presentation followed the mean ± standard deviation (SD) format. One-way ANOVA served for statistical comparisons, and $p < 0.05$ reported statistical significance.

3.Results and discussion

3.1. Preparation and characterization

Albumin contains a high proportion of negatively charged amino acids, facilitating the binding of metal cations to albumin through electrostatic adsorption. Under alkaline conditions, albumin denatures, releasing a significant number of amino acids, among which cysteine serves as a valuable source of sulfur for the metal sulfides [31, 32]. Using the biomineralization method, Bi_2S_3 and Gd_2O_3 were generated. The abundant functional groups on their surfaces provided sites for subsequent surface modification of the nanomaterials. FA-functionalized Bi_2S_3-Gd_2O_3@BSA was synthesized by activating the carboxyl group of FA, which subsequently reacted with the amino groups on the BSA surface to form stable amide bonds.

Transmission electron microscopy showed that the Bi_2S_3-Gd_2O_3@BSA particles had a spherical morphology, and the average diameter was 29 ± 5 nm. Additionally, its lattice stripes were consistent with d211 of orthorhombic Bi_2S_3 and d420 of cubic Gd_2O_3, as observed using HRTEM (Fig. 1a and b). Hydration particle size analysis demonstrated that the size of Bi2S3-Gd2O3@BSA particles increased gradually from 43.7 nm to 91.24 nm following targeted functionalization. The potential of the nanomaterial also changed, particularly after the modification with FA, shifting from -30.6 mV to -18.5 mV (Fig. 1c, d, and e).

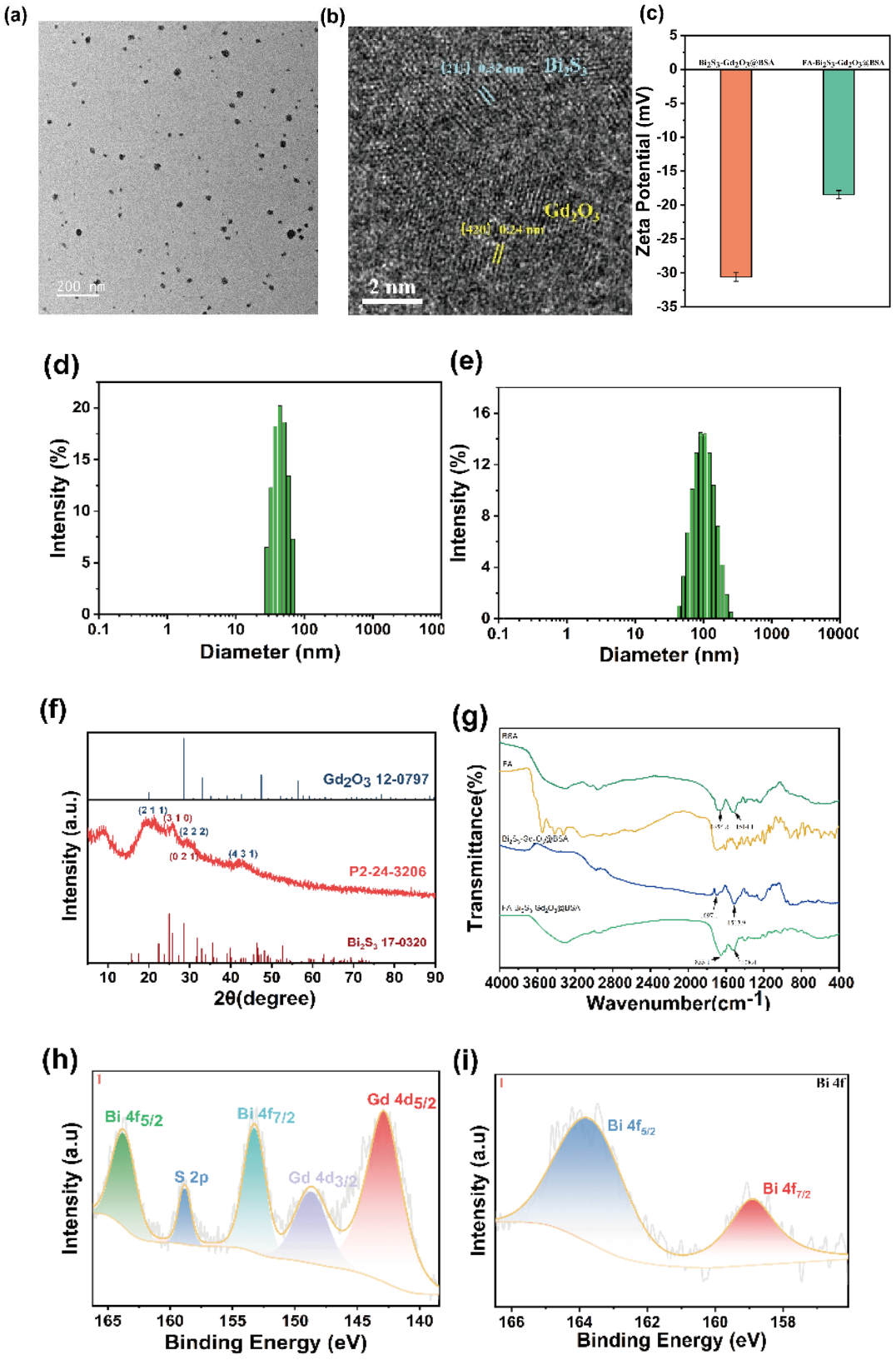

Fig. 1. (a) (a) TEM image of Bi_2S_3-Gd_2O_3@BSA; (b) HRTEM lattice fringing of Bi_2S_3-Gd_2O_3@BSA; (c) Zeta potential maps before and after modification (d) Hydrated particle size of Bi_2S_3-Gd_2O_3@BSA; (e) Hydrated particle size of FA-Bi_2S_3-Gd_2O_3@BSA; (f) XRD plots of Bi_2S_3-Gd_2O_3@BSA; (g) FT-IR spectra of FA; BSA; Bi_2S_3-Gd_2O_3@BSA; FA-Bi_2S_3-Gd_2O_3@BSA; (h) XPS characterizations including full survey spectra of Bi_2S_3-Gd_2O_3@BSA; (i) Peak fitting diagram of Bi4f.

The X-ray diffraction (XRD) spectra of Bi_2S_3-Gd_2O_3@BSA exhibit diffraction peaks corresponding to orthorhombic Bi_2S_3 (JCPDS No. 17-0320) and cubic Gd_2O_3 (JCPDS No. 44-1246). The XRD spectra (Fig. 1f) also show diffraction peaks for the orthorhombic Bi_2S_3 phase (JCPDS No. 17-0320) and cubic Gd_2O_3 (JCPDS No. 44-1246). Fourier transform infrared spectroscopy (FTIR) was applied for analyzing Bi_2S_3-Gd_2O_3@BSA. (Fig. 1g), which revealed characteristic peaks of BSA at 1656.8 cm^{-1} and 1514.1 cm^{-1}. After BSA was denatured and modified with −SH for Bi_2S_3 preparation, the encapsulation effect was demonstrated by observing the absorption of BSA in the FTIR spectrum of Bi_2S_3-Gd_2O_3@BSA. Furthermore, the interaction between BSA and $Bi_2S_3$was indicated by the peak shifts of BSA to 1697.1 cm^{-1} and 1513.9 cm^{-1}, which facilitated the formation of Bi_2S_3-Gd_2O_3@BSA. After the conjugation of FA to the surface of Bi_2S_3-Gd_2O_3@BSA, the peaks at 1697.1 cm^{-1} and 1513.9 cm^{-1} in the Bi_2S_3-Gd_2O_3@BSA spectrum shifted to 1650.8 cm^{-1} and 1515.9 cm^{-1}. Additionally, several characteristic bands of FA were observed between 833.1 cm^{-1} and 1608.4 cm^{-1}. Additionally, the chemical composition of Bi_2S_3-Gd_2O_3@BSA was analyzed with XPS. According to analysis results, the Bi 4f 7/2 and Bi 4f 5/2 XPS spectral peaks of Bi_2S_3-Gd_2O_3@BSA were 153.28 eV and 163.83 eV, respectively, confirming the presence of Bi^{3+} in Bi_2S_3-Gd_2O_3@BSA (Fig. 1h and i). Furthermore, a characteristic peak corresponding to the S 2p orbitals of S^{2-} was identified at 158.83 eV, confirming the formation of Bi_2S_3. Additionally, the electronic binding energies for Gd 4d3/2 and Gd 4d5/2 were measured at 148.73 eV and 142.88 eV, respectively, further validating the presence of Gd_2O_3.

3.2. Photothermal conversion characteristics

To assess the photothermal heating capacity of FA- Bi_2S_3-Gd_2O_3@BSA, we prepared a range of aqueous dispersions with varying concentrations. Each sample underwent 10 min of laser irradiation. During this procedure, thermal imaging cameras were employed for the in-time monitoring and recording of the temperature changes. As illustrated in Fig. 2a, the photothermal warming effect became more pronounced with increased treatment time and higher concentrations of the material dispersion. When Bi^{3+} concentration was 160 μg/mL, the temperature of the dispersion system can reach approximately 64.4 °C. This elevated temperature, specifically around 50 °C, is sufficient for inducing cancer cell death and exerting an anti-tumor effect. The calculated photothermal conversion efficiency was 30%, based on previously reported methodologies. Moreover, photothermal cyclic stability is an essential factor in assessing PTAs. Therefore, a dispersion of 120 μg/mL Bi nanoparticles was used to evaluate photothermal stability. The dispersion was subjected to irradiation followed by natural cooling for 10 minutes in each cycle, for a total of five cycles. As shown in Fig. 2c, after five cycles, the FA-Bi_2S_3-Gd_2O_3@BSA dispersion exhibited minimal temperature changes, confirming its good photothermal stability. Fig. 2e presents the near-infrared map of the FA-Bi_2S_3-Gd_2O_3@BSA dispersion. With prolonged irradiation time and increased dispersion concentration, the photothermal imaging signal became more pronounced, significantly exceeding that of pure water. This finding suggests that the material exhibits excellent photothermal imaging properties, enabling real-time monitoring and documentation of temperature changes in the tumor region throughout photothermal therapy.

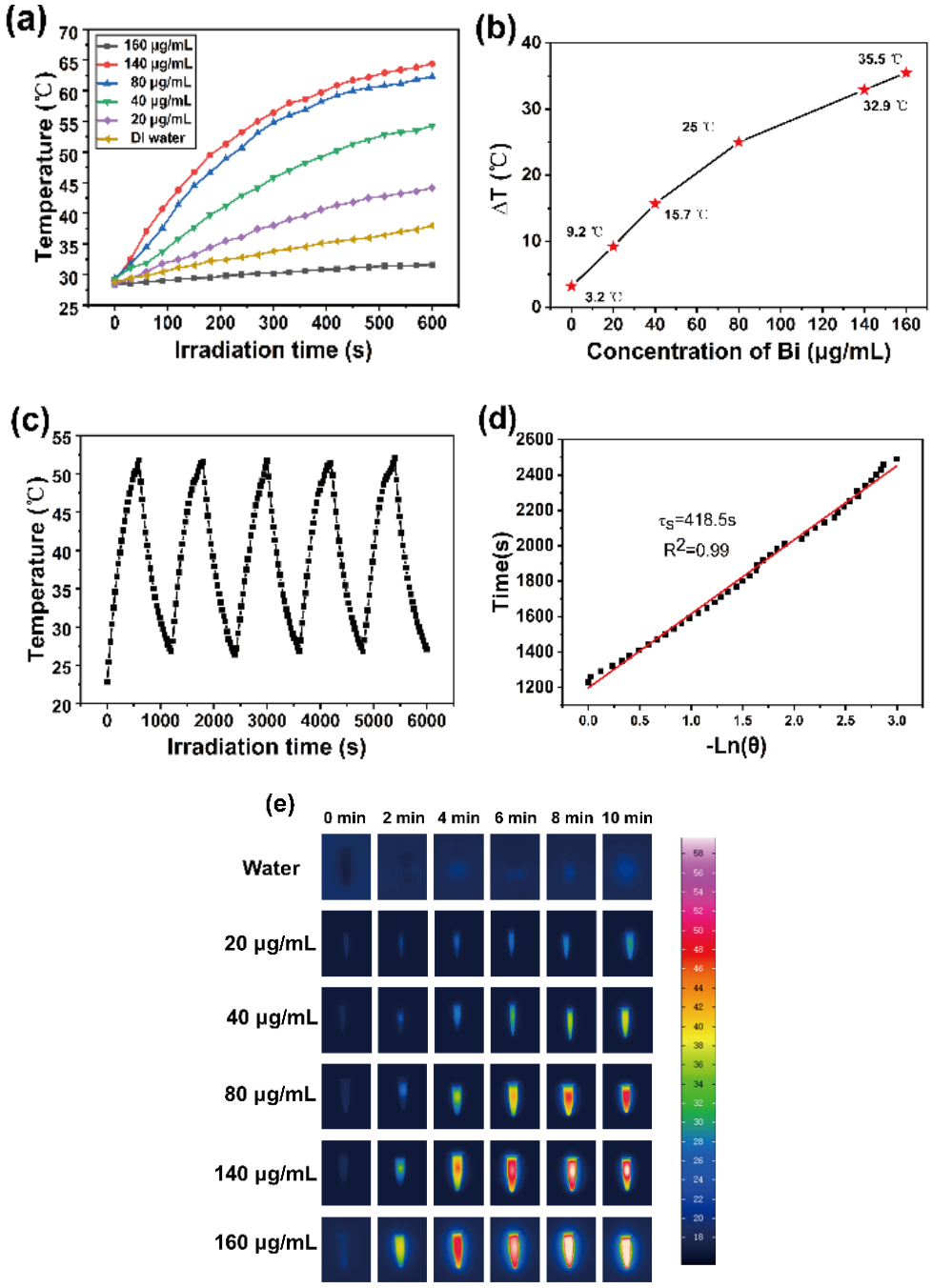

Fig. 2. (a) Heating-up curves of nanomaterial dispersions with different concentrations; (b) Temperature difference curves; (c) Temperature increase and natural cooling process of FA-Bi_2S_3-Gd_2O_3@BSA under laser irradiation; (d) Fitted curves of -ln (θ) versus time during natural cooling process (e) Elevated temperature infrared thermograms.

3.3. Biosafety of Bi_2S_3-Gd_2O_3@BSA

A standard CCK-8 assay assisted in evaluating the in vitro cytotoxicity of FA- Bi_2S_3-Gd_2O_3@BSA. (Fig. 3a). With the Bi^{3+} concentration increasing to 300 μg/mL, the survival rate of HT-29 cells continued to exceed 90%, and this rate remained above 85% even after 48 hours of incubation. These results indicate that the material exhibits low toxicity, making it suitable for

further cell experiments. The hemolysis test results (Fig. 4b) reveal that the solution from the positive control group (deionized water-treated) maintained a red color following centrifugation.

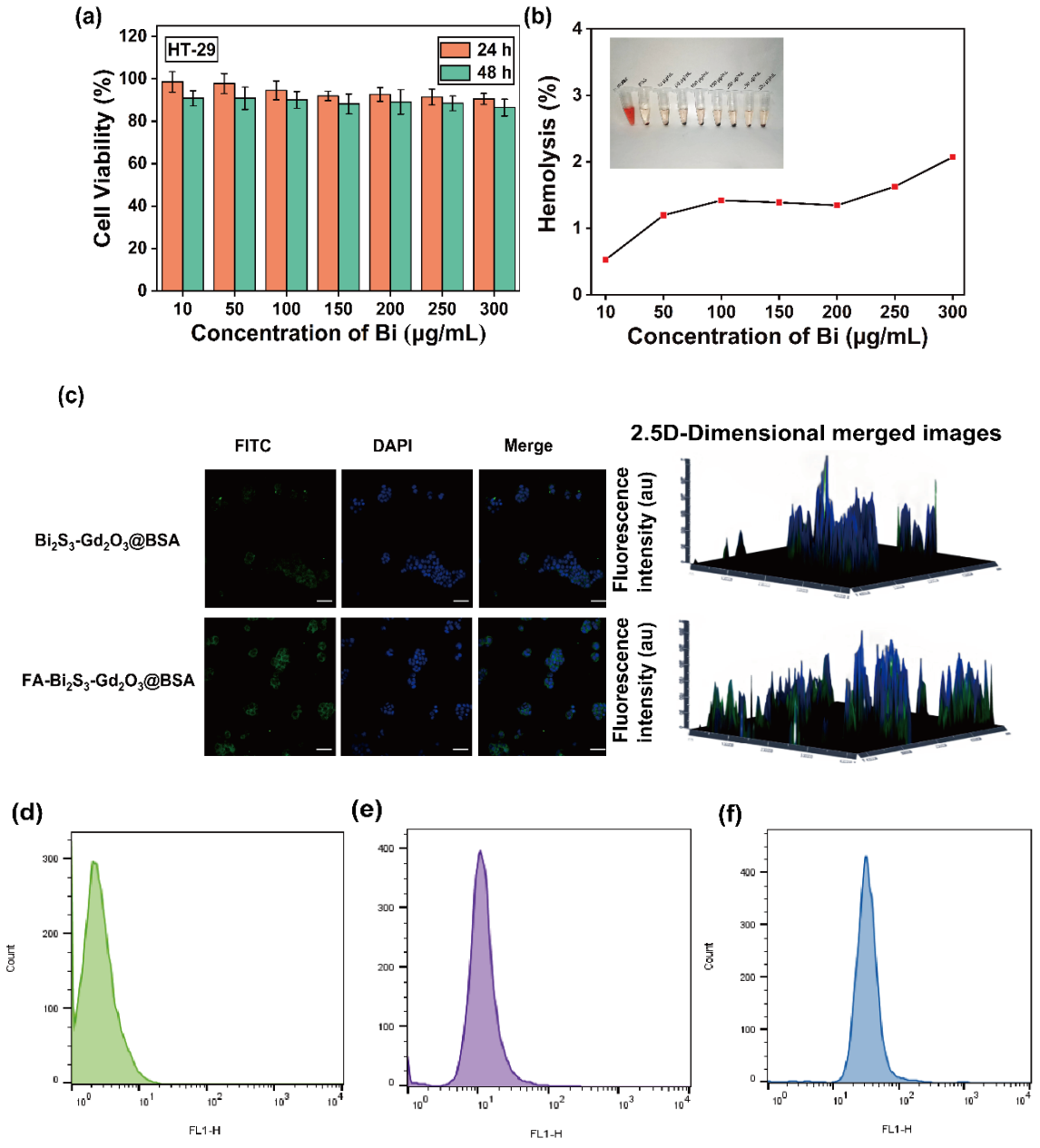

Fig. 3. (a) Cytotoxicity of HT-29 cells after 24 and 48 h of treatment with FA-Bi_2S_3-Gd_2O_3@BSA; (b) Hemolysis rate of erythrocytes with FA-Bi_2S_3-Gd_2O_3@BSA (inset shows hemolysis graph) (c) Confocal fluorescence image of HT-29 cells after incubation with nanomaterials (scale bar: 50 μm); (d) The green fluorescence of HT-29 cells in PBS group, (e) Bi_2S_3-Gd_2O_3@BSA group (f) and FA-Bi_2S_3-Gd_2O_3@BSA group was detected by flow cytometry.

In contrast, the RBCs in the negative control group settled at the bottom of the tube. This observation suggests that hemolysis occurred in the RBCs of the positive control group. Co-incubation of the erythrocyte suspension with various concentrations of FA-Bi_2S_3-Gd_2O_3@BSA was

followed by the centrifugation, resulting in erythrocyte sedimentation at the bottom of the centrifuge tube. The hemolysis rate was < 5%, even at a concentration of 300 μg/mL, indicating minimal hemolysis and demonstrating favorable hemocompatibility in vivo.

3.4. Cellular uptake experiments

Using unmodified Bi_2S_3-Gd_2O_3@BSA-FITC as a control, HT-29 cells were incubated with FA-Bi_2S_3-Gd_2O_3@BSA-FITC and Bi_2S_3-Gd_2O_3@BSA-FITC for 4 hours, after which the cells were imaged using CLSM (Fig. 3c). The merged image indicates that the yellow-green fluorescence of FA-Bi_2S_3-Gd_2O_3@BSA-FITC nanomaterials was significantly greater than that of Bi_2S_3-Gd_2O_3@BSA-FITC. According to quantitative flow cytometry analysis (Fig. 3d-f), FA-Bi_2S_3-Gd_2O_3@BSA-FITC had a stronger fluorescence intensity versus Bi_2S_3-Gd_2O_3@BSA-FITC. In summary, the results indicate that FA-Bi_2S_3-Gd_2O_3@BSA nanomaterials effectively target HT-29 cells, and that FA modification enhances cellular uptake.

3.5. The effect of photothermal therapy on tumor cells

Given the favorable cytotoxicity, the photothermal cell-killing performance of Bi_2S_3-Gd_2O_3@BSA and FA-Bi_2S_3-Gd_2O_3@BSA was evaluated. A concentration of 120 μg/mL Bi^{3+} was used for both Bi_2S_3-Gd_2O_3@BSA and FA-Bi_2S_3-Gd_2O_3@BSA dispersions, which were co-incubated with HT-29 cells in 96-well plates for 24 hours. Following this, the samples underwent 0, 3, 7, and 10 min of irradiation with an 808 nm laser (1 W/cm²). Upon completion of the irradiation, the CCK-8 assay was employed to assess the cell viability in each group. According to Fig. 4a, the relative cell viability gradually decreased with prolonged irradiation time, with cell viability reaching approximately 28.2% and 12.5% after 10 minutes of irradiation, indicating that the killing effect of FA-Bi_2S_3-Gd_2O_3@BSA was superior to that of Bi_2S_3-Gd_2O_3@BSA on HT-29 cancer cells. To directly assess the photothermal therapeutic effects of Bi2S3-Gd2O3@BSA and FA-Bi2S3-Gd2O3@BSA at the cellular level, cells were stained with Calcein AM and Propidium Iodide (PI) respectively for live cells and dead cells. Observations were made using an inverted fluorescence microscope to capture images. As illustrated in Fig. 4c, HT-29 cells co-incubated with Bi_2S_3-Gd_2O_3@BSA and FA-Bi_2S_3-Gd_2O_3@BSA displayed significant cell death following laser irradiation, with the killing effect being more pronounced in the FA-Bi_2S_3-Gd_2O_3@BSA group.

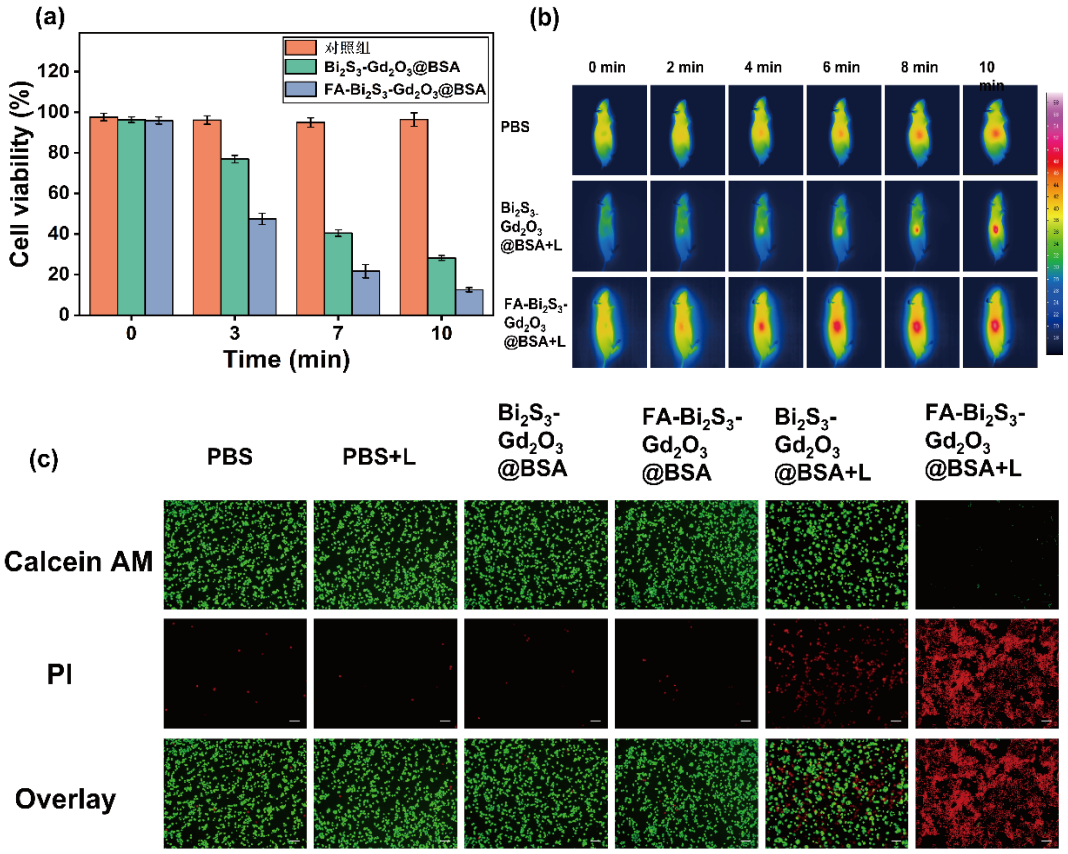

Fig. 4. (a) Cell survival of Bi_2S_3-Gd_2O_3@BSA and FA-Bi_2S_3-Gd_2O_3@BSA solutions after laser irradiation; (b) Infrared thermograms of mice; (c) Inverted fluorescence plots of live and dead cells after treatment in different ways (Scale bar: 50 μm).

3.6. MRI imaging

Subsequently, the MRI imaging performance of FA-Bi_2S_3-Gd_2O_3@BSA was evaluated by measuring its longitudinal relaxation time at various concentrations. A linear plot of the relaxation rate ($1/T_1$) versus concentration was constructed to determine the slope of the line, representing the longitudinal relaxation rate (r_1). As shown in Fig. 5b, the longitudinal relaxation rate of FA-Bi_2S_3-Gd_2O_3@BSA was 10.057 $mM^{-1}\cdot s^{-1}$, and T_1-weighted imaging became progressively brighter with increasing solution concentration. MRI images of the mice indicated notable alterations in the tumor region one hour after the injection of FA-Bi_2S_3-Gd_2O_3@BSA. The highest signal intensity was observed 3 h post-injection, after which there was a gradual decline in signal strength. (Fig. 5a). These results further indicate that the nano delivery system loaded with the folate ligand FA effectively targets the tumor site for enrichment after entering the organism.

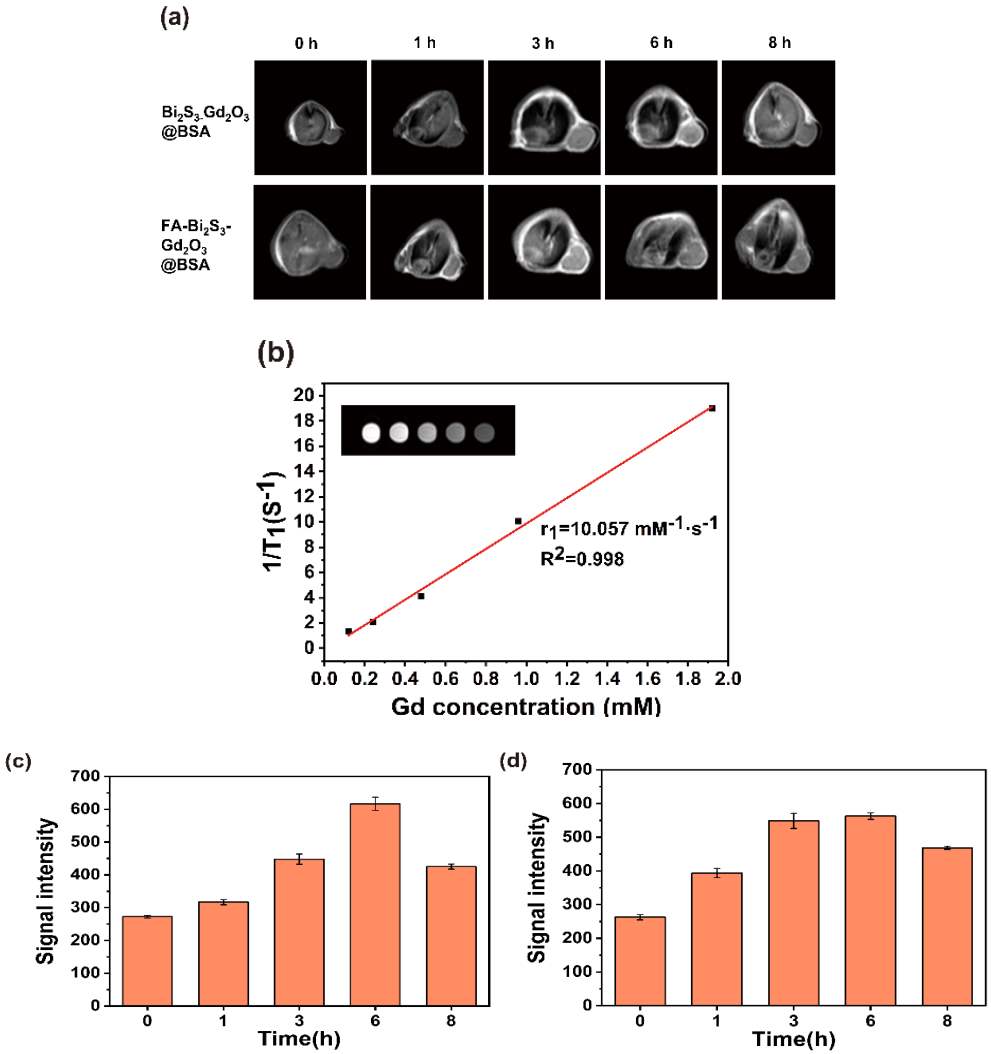

Fig. 5. (a) Time point-based in vivo MR images of mice after intravenous injection of Bi_2S_3-Gd_2O_3@BSA and FA-Bi_2S_3-Gd_2O_3@BSA solutions; (b) A series of concentrations of FA-Bi_2S_3-Gd_2O_3@BSA solution 1/T1 fitting curves (insets are solution T1-weighted images); (c) The average MRI signal intensity of the tumor in the Bi_2S_3-Gd_2O_3@BSA group; (f) and FA-Bi_2S_3-Gd_2O_3@BSA group.

3.7. Internal photothermal therapy

Following 2 h of intravenous administration of the Bi_2S_3-Gd_2O_3@BSA solution (5 mg/mL), the photothermal effect of Bi_2S_3-Gd_2O_3@BSA was monitored using an infrared camera. In the FA-Bi_2S_3-Gd_2O_3@BSA group, the tumor temperature reached 46.8 °C within 10 minutes of exposure to the 808 nm laser. In contrast, the temperature in the Bi_2S_3-Gd_2O_3@BSA group was 42.5 °C, both of which exceeded the control group's temperature of 35.9 °C by a significant margin. (Fig. 4b). Achieving a temperature of 42 °C is sufficient for tumor treatment; although the non-target group also reached 42 °C within 10 minutes, the target group enriched more tumor areas simultaneously, demonstrating a better warming effect. These findings suggest that Bi_2S_3-Gd_2O_3@BSA serves as a promising PTA for applications within near-infrared biological windows. Mice with tumors were assigned to six different groups in a random manner.: the control group (PBS only), Bi_2S_3-Gd_2O_3@BSA group (Bi_2S_3-Gd_2O_3@BSA only), FA-Bi_2S_3-Gd_2O_3@BSA group (FA-Bi_2S_3-Gd_2O_3@BSA only), NIR group (808 nm laser irradiation only), Bi_2S_3-Gd_2O_3@BSA + NIR group (Bi_2S_3-Gd_2O_3@BSA + 808 nm laser irradiation), and FA-Bi_2S_3-Gd_2O_3@BSA + NIR group (FA-

Bi_2S_3-Gd_2O_3@BSA + 808 nm laser irradiation). According to Fig. 6a and 6c, the FA-Bi_2S_3-Gd_2O_3@BSA + NIR group exhibited the smallest tumor volume and weight compared to the other six groups, indicating effective inhibition and elimination of tumor growth by FA-Bi_2S_3-Gd_2O_3@BSA following treatment with near-infrared laser irradiation. Concurrently, H&E staining of tumors (Fig. 6f) demonstrated that FA-Bi_2S_3-Gd_2O_3@BSA exhibited a robust near-infrared laser-triggered photothermal effect.

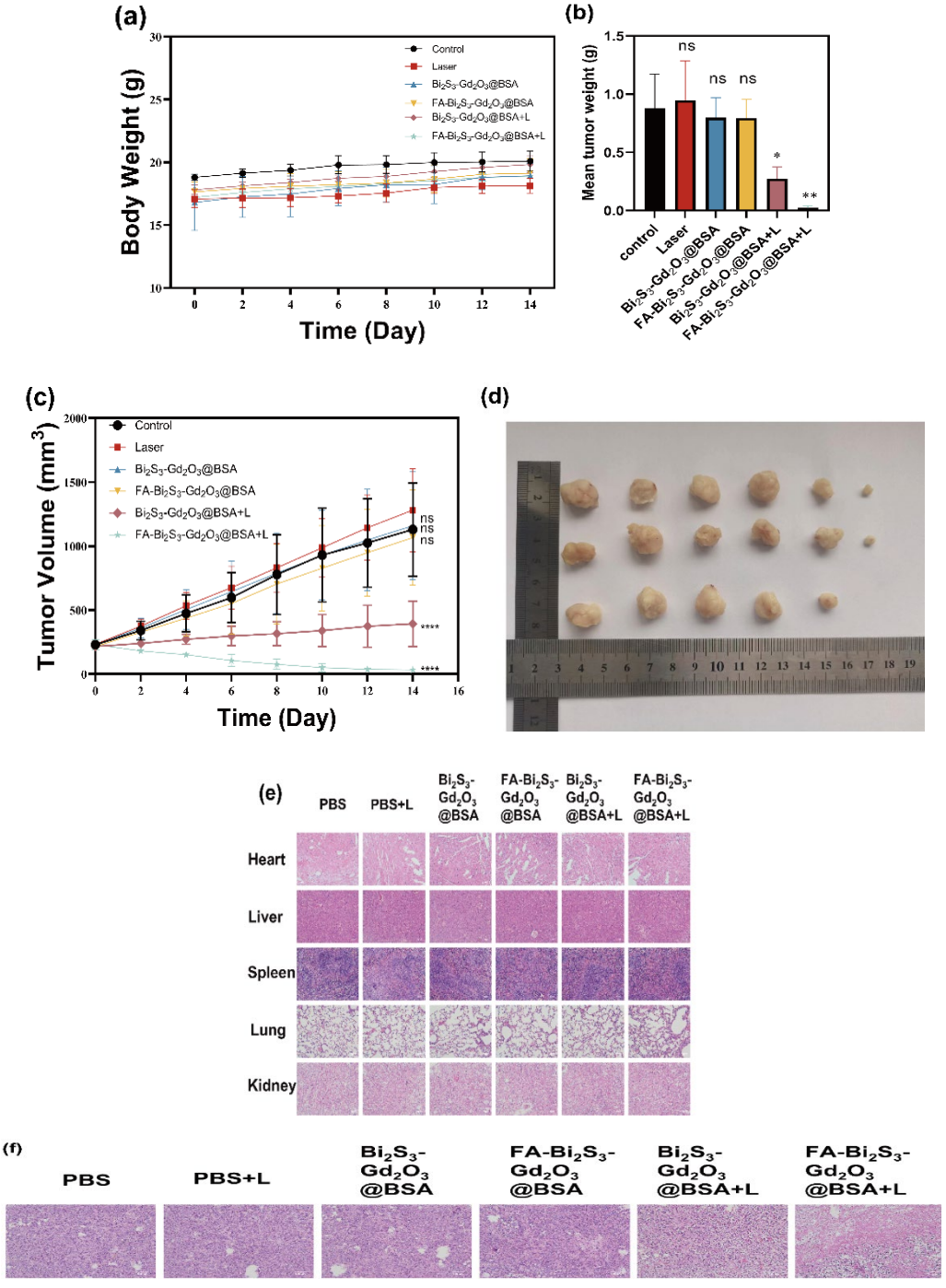

*Fig. 6. (a) Tumor volume growth graph in mice; (b) Weights of mice in 6 treatment groups; (c) An obvious reduction on the final mean tumor weight after two weeks of treatment in the experimental groups (****P < 0.0001, **P < 0.01 and *P < 0.1); (d) Tumor treatment effect diagram; (e) H&E staining images of major organs—such as the heart, liver, spleen, lungs, and kidneys from hormone-treated mice (scale bar: 100 μm); (f) H&E-stained sections of tumor tissues from each group at the conclusion of treatment (scale bar: 100 μm).*

4. Conclusion

In summary, BSA-stabilized Bi_2S_3-Gd_2O_3@BSA was synthesized for MRI imaging diagnosis and photothermal therapy of tumors. Traditional nanomaterials typically penetrate tumors by virtue of the enhanced permeability and retention (EPR) effect. In contrast, folate receptors (FR) are preferentially overexpressed in cancer cells versus normal cells [33]. Folic acid (FA) serves as a complementary ligand for FR receptors, exhibiting strong binding affinity [34-36]. Therefore, FA was chosen for surface modification to complete targeted delivery pertaining to the nanomaterials. The in vitro and in vivo risks of BSA-stabilized Bi_2S_3-Gd_2O_3@BSA were carefully evaluated through body weight fluctuation, hemolysis assays, and cytotoxicity tests, demonstrating satisfactory biosafety. Although Bi_2S_3 itself did not exhibit therapeutic effects, its excellent photothermal conversion efficiency effectively eliminated tumors, resulting in gradual tumor volume reduction in hormone-treated mice after 14 days of treatment. Additionally, Bi_2S_3-Gd_2O_3@BSA demonstrated strong performance in T_1-weighted MR imaging. Under the guidance of FA, Bi_2S_3-Gd_2O_3@BSA effectively aggregated in the tumor region. This study aims to create a new multifunctional diagnostic nano-agent intended for MRI-guided photothermal therapy in cancer treatment.

Acknowledgments

This work completed with the support from the Qiqihar Academy of Medical Sciences Fund Project (No. QMSI2022M-07), the Qiqihar Science and Technology Bureau (No. LHYD-202013).

Author contributions

Conceptualization, Wenbo Duan; Data curation, Tonghui Yi; Funding acquisition, liping zhang; Methodology, Yonggang Wan; Resources, benhan Zhang; Software, Jianlei Xue and Guo Xu; Supervision, Liguo Hao; Validation, Datong Chen; Visualization, Jie Wang; Writing – review & editing, Qian Lu.

Data availability statement

The data and materials from this study are available from the first author upon reasonable request.

Conflict of interest

The authors declare that they have no conflict of interest.

Ethical approval

The study adhered to the guidelines of the Declaration of Helsinki, and obtained the approval of the institutional animal care and use committee of Qiqihar Medical university (approval No. QMU-AECC-2022-89). All animal housing and experiments strictly followed the institutional guidelines for the care and use of laboratory animals, adhering to the ARRIVE guidelines.

References

[1] Y. Xi, P. Xu, Translational oncology 14(10), 101174 (2021); https://doi.org/10.1016/j.tranon.2021.101174

[2] R. Jiang, L. Hang, W. Li, H. Ling, H. Wang, Q. Lei, H. Su, Y. Chen, X. Ma, G. Jiang, ACS Applied Nano Materials 7(1), 1450-1461 (2023); https://doi.org/10.1021/acsanm.3c05733

[3] X. Wu, H. Liang, C. Li, D. Zhou, R. Liu, RSC advances 13(41), 29061-29069 (2023); https://doi.org/10.1039/D3RA04779B

[4] L. Zhang, Z. Yang, W. He, J. Ren, C.-Y. Wong, Journal of Colloid and Interface Science 599(543-555 (2021); https://doi.org/10.1016/j.jcis.2021.03.173

[5] P.S. Hegde, D.S. Chen, Immunity 52(1), 17-35 (2020); https://doi.org/10.1016/j.immuni.2019.12.011

[6] W. Kong, Q. Wang, G. Deng, H. Zhao, L. Zhao, J. Lu, X. Liu, Dalton transactions (Cambridge, England : 2003) 49(7), 2209-2217 (2020); https://doi.org/10.1039/C9DT04867G

[7] Y. Wang, X. Liu, G. Deng, J. Sun, H. Yuan, Q. Li, Q. Wang, J. Lu, Nanoscale 10(6), 2866-2875 (2018); https://doi.org/10.1039/C7NR09237G

[8] Z. Zhou, X. Wang, H. Zhang, H. Huang, L. Sun, L. Ma, Y. Du, C. Pei, Q. Zhang, H. Li, L. Ma, L. Gu, Z. Liu, L. Cheng, C. Tan, Small 17(12), e2007486 (2021); https://doi.org/10.1002/smll.202007486

[9] H. Liu, W. Lin, L. He, T. Chen, Biomaterials 226, 119545 (2020); https://doi.org/10.1016/j.biomaterials.2019.119545

[10] B. Qiao, Y. Luo, H.B. Cheng, J. Ren, J. Cao, C. Yang, B. Liang, A. Yang, X. Yuan, J. Li, L. Deng, P. Li, H.T. Ran, L. Hao, Z. Zhou, M. Li, Y. Zhang, P.S. Timashev, X.J. Liang, Z. Wang, ACS nano 14(10), 12652-12667 (2020); https://doi.org/10.1021/acsnano.0c00771

[11] L. Zhou, L. Chen, X. Hu, Y. Lu, W. Liu, Y. Sun, T. Yao, C. Dong, S. Shi, Communications biology 3(1), 343 (2020); https://doi.org/10.1038/s42003-020-1070-6

[12] J. Li, J. Wang, J. Zhang, T. Han, X. Hu, M.M.S. Lee, D. Wang, B.Z. Tang, Advanced materials (Deerfield Beach, Fla.) 33(51), e2105999 (2021); https://doi.org/10.1002/adma.202105999

[13] Z. Tang, Y. Hou, S. Huang, N.S. Hosmane, M. Cui, X. Li, M. Suhail, H. Zhang, J. Ge, M.Z. Iqbal, X. Kong, Acta biomaterialia 177, 431-443 (2024); https://doi.org/10.1016/j.actbio.2024.01.041

[14] S. Duan, Y. Hu, Y. Zhao, K. Tang, Z. Zhang, Z. Liu, Y. Wang, H. Guo, Y. Miao, H. Du, D. Yang, S. Li, J. Zhang, RSC advances 13(21), 14443-14460 (2023); https://doi.org/10.1039/D3RA02620E

[15] X. Chang, X. Tang, J. Liu, Z. Zhu, W. Mu, W. Tang, Y. Zhang, X. Chen, Advanced Functional Materials 33(35), (2023); https://doi.org/10.1002/adfm.202303596

[16] S.F.A. Sugito, A. Wibrianto, J.Y. Chang, M.Z. Fahmi, S.Q. Khairunisa, S.C.W. Sakti, M.A. Ahmad, L. Hwei Voon, Y.L. Nikmah, Dalton transactions (Cambridge, England : 2003) 53(27), 11368-11379 (2024); https://doi.org/10.1039/D4DT01123F

[17] W. Liu, Y. Wang, Y. Wang, X. Li, K. Qi, J. Wang, H. Xu, ACS applied materials & interfaces 15(1), 236-248 (2023); https://doi.org/10.1021/acsami.2c14436

[18] X.-S. Zhang, J.-S. Wei, J.-W. Chen, K. Cheng, F. Zhang, G. Ashraf, Y. Li, X.-L. Hou, R.-Y. Zhang, Y.-G. Hu, X.-Q. Yang, W. Chen, B. Liu, Y.-D. Zhao, Chemical Engineering Journal 433((2022); https://doi.org/10.1016/j.cej.2021.133196

[19] W. Xie, Y. Lu, Y. Yuan, L. Xiao, J. Liu, H. Song, R. Niu, Y. Liu, J. Lin, ACS biomaterials science & engineering (2024).

[20] W. Zhang, J. Li, L. Chen, H. Chen, L. Zhang, Colloids and surfaces. B, Biointerfaces 230, 113529 (2023); https://doi.org/10.1016/j.colsurfb.2023.113529

[21] M. Du, X. He, D. Wang, Z. Jiang, X. Zhao, J. Shen, Acta biomaterialia 179, 300-312 (2024); https://doi.org/10.1016/j.actbio.2024.03.014

[22] Y. Wang, S. Song, T. Lu, Y. Cheng, Y. Song, S. Wang, F. Tan, J. Li, N. Li, Biomaterials 220, 119405 (2019); https://doi.org/10.1016/j.biomaterials.2019.119405

[23] D. Sang, K. Wang, X. Sun, Y. Wang, H. Lin, R. Jia, F. Qu, ACS applied materials & interfaces 13(8), 9604-9619 (2021); https://doi.org/10.1021/acsami.0c21284

[24] J. You, L. Liu, W. Huang, I. Manners, H. Dou, ACS applied materials & interfaces 13(27), 32599 (2021); https://doi.org/10.1021/acsami.1c11480

[25] L. Palanikumar, M. Kalmouni, T. Houhou, O. Abdullah, L. Ali, R. Pasricha, S. Thomas, A.J. Afzal, F.N. Barrera, M. Magzoub, bioRxiv : the preprint server for biology (2023).

[26] A. Yilmazer, Z. Eroglu, C. Gurcan, A. Gazzi, O. Ekim, B. Sundu, C. Gokce, A. Ceylan, L. Giro, M.A. Unal, F. Arı, A. Ekicibil, O. Ozgenç Çinar, B.I. Ozturk, O. Besbinar, M. Ensoy, D. Cansaran-Duman, L.G. Delogu, O. Metin, Materials today. Bio 23, 100825 (2023); https://doi.org/10.1016/j.mtbio.2023.100825

[27] J. Lv, X. Wang, X. Zhang, R. Xu, S. Hu, S. Wang, M. Li, Asian journal of pharmaceutical sciences 18(3), 100798 (2023); https://doi.org/10.1016/j.ajps.2023.100798

[28] Y. Qi, S. Ren, J. Ye, Y. Tian, G. Wang, S. Zhang, L. Du, Y. Li, Y. Che, G. Ning, Acta biomaterialia 143, 445-458 (2022); https://doi.org/10.1016/j.actbio.2022.02.034

[29] Z. Guo, Y. Liu, H. Zhou, K. Zheng, D. Wang, M. Jia, P. Xu, K. Ma, C. Cui, L. Wang, Colloids and surfaces. B, Biointerfaces 184, 110546 (2019); https://doi.org/10.1016/j.colsurfb.2019.110546

[30] P. Zhang, L. Wang, X. Chen, X. Li, Q. Yuan, Frontiers in pharmacology 12, 795012 (2021); https://doi.org/10.3389/fphar.2021.795012

[31] J.M. Irache, M. Merodio, A. Arnedo, M.A. Camapanero, M. Mirshahi, S. Espuelas, Mini reviews in medicinal chemistry 5(3), 293-305 (2005);

https://doi.org/10.2174/1389557053175335

[32] C. Weber, C. Coester, J. Kreuter, K. Langer, International journal of pharmaceutics 194(1), 91-102 (2000); https://doi.org/10.1016/S0378-5173(99)00370-1

[33] A. Scomparin, S. Salmaso, A. Eldar-Boock, D. Ben-Shushan, S. Ferber, G. Tiram, H. Shmeeda, N. Landa-Rouben, J. Leor, P. Caliceti, A. Gabizon, R. Satchi-Fainaro, Journal of controlled release : official journal of the Controlled Release Society 208, 106-120 (2015); https://doi.org/10.1016/j.jconrel.2015.04.009

[34] H. Huang, D.P. Yang, M. Liu, X. Wang, Z. Zhang, G. Zhou, W. Liu, Y. Cao, W.J. Zhang, X. Wang, International journal of nanomedicine 12, 2829-2843 (2017); https://doi.org/10.2147/IJN.S128270

[35] Y. Huang, Z. Xue, S. Zeng, ACS applied materials & interfaces 12(28), 31172-31181 (2020); https://doi.org/10.1021/acsami.0c07372

[36] J. Wang, L. Zhang, H. Xin, Y. Guo, B. Zhu, L. Su, S. Wang, J. Zeng, Q. Chen, R. Deng, Z. Wang, J. Wang, X. Jin, S. Gui, Y. Xu, X. Lu, Acta biomaterialia 152, 453-472 (2022); https://doi.org/10.1016/j.actbio.2022.08.071